13. A solid-medium high-pressure deformation apparatus such as the Griggs apparatus can be used to ~3 Gpa, whereas a gas-medium high-pressure deformation apparatus such as the Paterson apparatus can be used only to ~0.5 GPa. This makes a large difference in water fugacity: ~13 GPa (at 2-GPa confining pressure and 1473 K) with a solid-medium apparatus, and ~0.6 GPa (at 0.5-GPa confining pressure and 1473 K) with a gas-medium apparatus.
14. For this purpose, a single crystal of olivine with the orientation [010] parallel to the compression axis was placed near the specimen. Absorption of the infrared beam at ~3000 to 3800 cm^{-1} of this single crystal of olivine was measured with a FTIR spectrometer, and the calibration by Paterson (*35*) was used to calculate water content from the absorption coefficient.
15. D. L. Kohlstedt, H. Keppler, D. C. Rubie, *Contrib. Mineral. Petrol.* **123**, 345 (1996).
16. Rotation of a strain marker and the change in sample thickness were measured after each experiment. The shear strain, γ, was calculated from the rotation angle of a strain marker, θ, as $\gamma = \tan\theta$, and the shortening strain, ϵ, was calculated from $\epsilon = \Delta h/h$ where h is the initial sample thickness and Δh is the change in sample thickness.
17. Measurement of a stress magnitude in samples deformed by a solid-medium apparatus is not trivial. Measurements by an external load-cell have very large errors and do not provide reliable values of stress. We used high-resolution dislocation density measurements to estimate the stress magnitude (*36*). Values of stress in Table 1 are obtained from the measurements of dislocation densities and have uncertainties of ~±10 to 15% (*21*). This technique works for type-A, -C, and -D samples, but not for type-B samples in which dislocation density is highly heterogeneous. Consequently, for type-B samples, a stress estimate based on flow laws was also used. The olivine flow law under water-rich conditions determined by Karato and Jung (*37*) was used to estimate the magnitude of stress from known temperature, pressure, strain rate, and water fugacity.
18. The effects of dynamic recrystallization to enhance fabric development have been demonstrated by Zhang and Karato (*2*). Bystricky *et al.* (*38*) reported much more sluggish kinetics of development of LPO, which is probably due to the slow kinetics of recrystallization at low temperature (1473 K) and water-poor conditions. Their results are consistent with the results obtained by Zhang *et al.* (*39*).
19. Carter and Avé Lallemant (*40*), Bystricky *et al.* (*38*), and Zhang *et al.* (*39*) reported another type of fabric (here called type-D) in which olivine [100] forms a well-defined maximum parallel to the shear direction, but in which other orientations make a girdle.
20. S. Karato, *Tectonophysics* **168**, 255 (1989).
21. H. Jung, S. Karato, *J. Struct. Geol.* **23**, 1337 (2001).
22. Our TEM observations show approximately the same number of **b** = [100] and **b** = [001] dislocations in "dry" samples, but most of the dislocations in "wet" samples (both type-B and type-C samples) have **b** = [001] Burgers vector. The **b** = [001] dislocations are mostly straight screws, indicating a high Peierls barrier.
23. We use the method described by Montagner and Nataf (*41*) to calculate V_{SH}/V_{SV} anisotropy.
24. Stress magnitude in Earth's upper mantle can be estimated from the microstructures of deformed rocks. Peridotites from typical rift-zone environment or xenoliths from ocean island basalts show stress magnitudes of ~1 to 10 MPa (*42*), whereas peridotites from collision zones (low temperature, high strain rates) show much higher stresses (~50 to 300 MPa) (*43*).
25. The transition from one type of fabric to another will occur when strain rates of two different slip systems coincide. Because the strain rate is a function primarily of temperature (T), stress (σ), and water content (C_{OH}), the boundary must be a surface in a three-dimensional space (T–σ–C_{OH}) defined by a function $f(T,\sigma,C_{OH}) = K$, where K is a constant. The temperatures in our experiments are close to those in the asthenosphere, and therefore boundaries in a σ–C_{OH} plane will be a good approximation to real boundaries in the hot regions of Earth (asthenosphere). From our experiments at low water content, we know that this boundary must pass a point $C_{OH} \cong 200$ ppm H/Si and $\sigma \cong 400$ MPa. Also, seismological observations show that the asthenosphere in a typical oceanic upper mantle [for which $C_{OH} \cong 800$ ppm H/Si (*33*) and $\sigma \cong 1$ to 10 MPa (*42*)] has a fabric corresponding to type-A, having $V_{SV} > V_{SH}$ anisotropy beneath mid-ocean ridges (*44*). Therefore, the boundary between type-A and type-C or type-D fabric must be $C_{OH} > 800$ ppm H/Si at $\sigma = 1$ to 10 MPa. Consequently, the boundary between type-C (or type-B) and type-A fabric must have a negative slope on this diagram. Such geometry of boundary is consistent with a microscopic model of plastic deformation involving motion of dislocations over a high Peierls barrier (*45*).
26. J. R. Möckel, *Leidse Geol. Med.* **42**, 61 (1969).
27. K. Frese, V. Trommsdorf, H.-R. Wenk, K. Kunze, *Deform. Mech. Rheol. Tectonics* **53**, 54 (2001).
28. G. Yoshino, *J. Sci. Hiroshima Univ. Ser. C* **3**, 343 (1961).
29. A. L. Littlejohn, H. J. Greenwood, *Can. J. Earth Sci.* **11**, 1288 (1974).
30. J.-G. Schilling, M. B. Bergeron, R. Evans, *Philos. Trans. R. Soc. London Ser. A* **297**, 147 (1980); D. H. Green, T. J. Falloon in *The Earth's Mantle*, I. Jackson, Ed. (Cambridge Univ. Press, Cambridge, 1998), p. 311.
31. D. R. Bell, G. R. Rossman, *Science* **255**, 1391 (1992).
32. S. Karato, *Nature* **319**, 309 (1986).
33. G. Hirth, D. L. Kohlstedt, *Earth Planet. Sci. Lett.* **144**, 93 (1996).
34. S. Karato, H. Jung, *Earth Planet. Sci. Lett.* **157**, 193 (1998).
35. M. S. Paterson, *Bull. Mineral.* **105**, 20 (1982).
36. S. Karato, K.-H. Lee, *Proc. 12th Int. Conf. Texture Mater.* (1999), p. 1546.
37. S. Karato, H. Jung, *Philos. Mag. Ser. A.*, in press.
38. M. Bystricky, K. Kunze, L. Burlini, J.-P. Burg, *Science* **290**, 1564 (2000).
39. S. Zhang, S. Karato, J. D. Fitz Gerald, U. H. Faul, Y. Zhou, *Tectonophysics* **316**, 133 (2000).
40. N. L. Carter, H. G. Avé Lallemant, *Geol. Soc. Am. Bull.* **81**, 2181 (1970).
41. J.-P. Montagner, H.-C. Nataf, *J. Geophys. Res.* **91**, 511 (1986).
42. J.-C. C. Mercier, *J. Geophys. Res.* **85**, 6293 (1980).
43. D. Jin, S. Karato, M. Obata, *J. Struct. Geol.* **20**, 195 (1998).
44. H.-C. Nataf, I. Nakanishi, D. L. Anderson, *J. Geophys. Res.* **91**, 7261 (1986).
45. H. J. Frost, M. F. Ashby, *Deformation Mechanism Maps* (Pergamon, Oxford, 1982), p. 167.
46. We thank K. Fischer, K. Frese, Z. Jiang, J.-P. Montagner, J. Park, and D. Wiens for discussion and K.-H. Lee for technical assistance. T. Hiraga performed the TEM study. Supported by NSF grants EAR-990387 and 0001955 (S.-i.K.) and by the University of Minnesota graduate school Doctoral Dissertation scholarship (H.J.).

3 May 2001; accepted 18 July 2001

Repeating Deep Earthquakes: Evidence for Fault Reactivation at Great Depth

Douglas A. Wiens and Nathaniel O. Snider

We have identified three groups of deep earthquakes showing nearly identical waveforms in the Tonga slab. Relocation with a cross-correlation method shows that each cluster is composed of 10 to 30 earthquakes along a plane 10 to 30 kilometers in length. Some of the earthquakes are colocated, demonstrating repeated rupture of the same fault, and one pair of events shows identical rupture complexity, suggesting that the temporal and spatial rupture pattern was repeated. Recurrence intervals show an inverse time distribution, indicating a strong temporal control over fault reactivation. Runaway thermal shear instabilities may explain temporally clustered earthquakes with similar waveforms located along slip zones weakened by shear heating. Earthquake doublets that occur within a few hours are consistent with events recurring before the thermal energy of the initial rupture can diffuse away.

Earthquakes with highly similar waveforms result when ruptures with identical focal mechanisms are located so close that complexly scattered waves show little difference between events (*1*). Similar earthquakes at shallow depths have been located accurately by cross-correlation techniques, thus allowing delineation of small features in the seismicity data (*2*) as well as detailed studies of earthquake recurrence and rupture properties (*3*, *4*). Similar deep earthquakes, although noted previously (*5*), have not been studied with modern methods. The study of possible repeating deep earthquakes may help to explain the mechanism that causes seismic rupture at depths of greater than 100 km (*6*–*10*).

Using regional broadband waveforms recorded by a 2-year seismograph deployment in 1993–95 (*11*), we identified three clusters of similar earthquakes in the deep Tonga slab. Seismograms from each cluster show nearly identical waveforms (Fig. 1), suggesting that the earthquakes must have similar focal mechanisms and locations. We used a cross-correlation technique to determine the relative arrival times of the regional P and S waves, as well as teleseismic P phases. The arrival times were then solved for the relative centroid positions and times of the events with a hypocentroidal decomposition method (*12*). The resulting arrival times and earth-

Department of Earth and Planetary Sciences, Washington University, St. Louis, MO 63130, USA.

quake locations are more accurate than standard methods, with relative residuals of about 0.1 s rather than 0.4 s for standard arrival time determinations. The 95% uncertainty ellipsoids have semiaxes on the order of ±1 to 3 km rather than 5 to 10 km for standard methods.

The Tonga deep earthquakes form a thin, faultlike planar feature in each of the three areas (Fig. 2). Such features have been identified previously (*13*), but the improved location technique demonstrates that the shear zones are at most only 2 or 3 km wide. We also identified several series of earthquakes that have nearly identical locations (Table 1). For this study, we define these colocated earthquakes as events that are separated by less than 3 km, because at this distance it becomes possible that the rupture zones of earthquakes from this data set [moment magnitude (M_w) 4.3 to 5.6]) might overlap or show repeated rupture. Three kilometers is also about the maximum uncertainty in the earthquake locations.

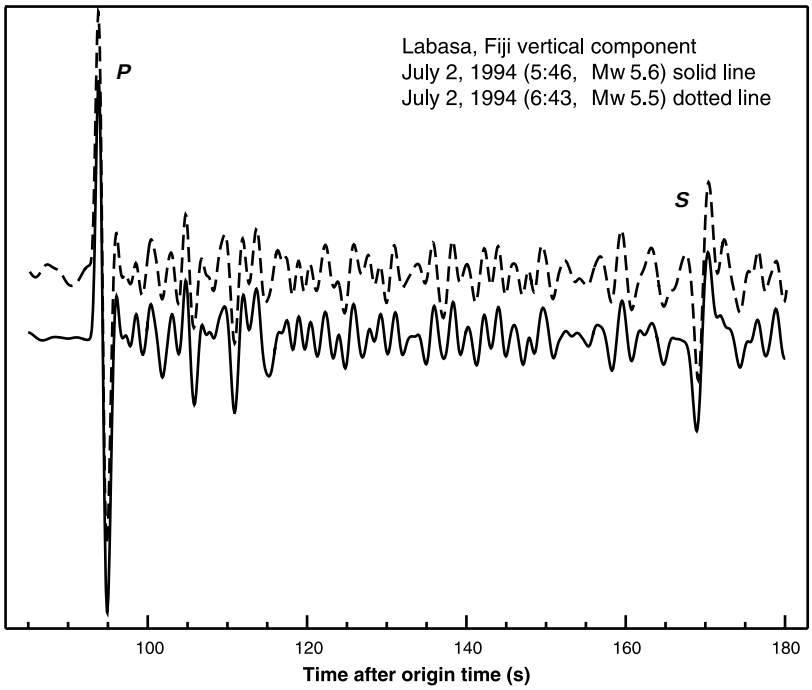

Fig. 1. Example of highly similar earthquake waveforms recorded at a temporary broadband seismic station in Fiji. The waveforms were aligned and low pass filtered at 0.5 Hz.

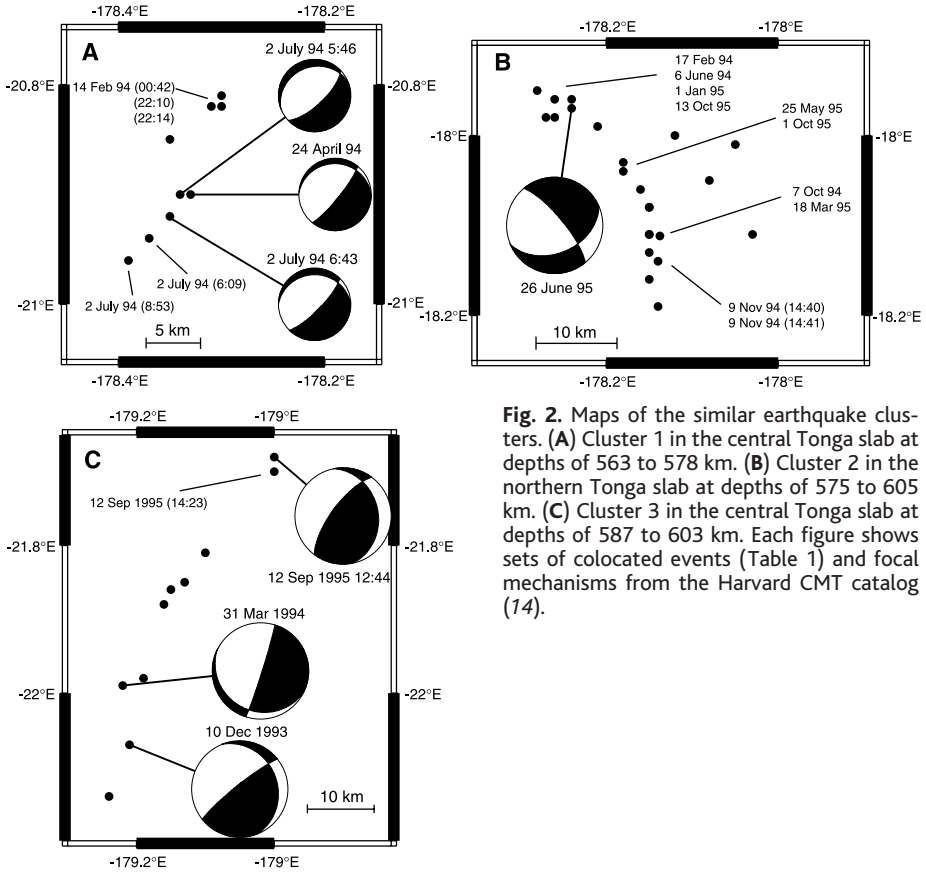

Fig. 2. Maps of the similar earthquake clusters. (**A**) Cluster 1 in the central Tonga slab at depths of 563 to 578 km. (**B**) Cluster 2 in the northern Tonga slab at depths of 575 to 605 km. (**C**) Cluster 3 in the central Tonga slab at depths of 587 to 603 km. Each figure shows sets of colocated events (Table 1) and focal mechanisms from the Harvard CMT catalog (*14*).

Cluster 1 consists of nine events that occurred within a 15 km by 15 km planar region in the central Tonga slab (Fig. 2A). The three largest events have nearly identical focal mechanisms determined by the Harvard Centroid Moment Tensor project (CMT) (*14*), showing dip-slip faulting on a steeply dipping plane aligned with the earthquake locations. Two of the largest events occurred less than an hour apart on 2 July 1994 (Table 1) and show centroids located 2 ± 2 km apart and displaced along the strike of the fault.

Cluster 2 consists of 22 earthquakes that occurred along a 25 km by 30 km vertical plane in the northern Tonga slab (Fig. 2B). The earthquakes are aligned with the near-vertical fault plane of the centroid moment tensor solution of the largest event (26 July 1995; moment magnitude 5.3). The strike of the faultlike structure is approximately aligned with the near-vertical Tonga slab in this location and is immediately to the south and about 25 km deeper than the epicenter of the 9 March 1994 (M_w 7.6) Tonga earthquake (*15*). Cluster 2 contains several sequences of colocated events, including two events separated by 55 s on 9 November 1994 (Table 1). Cluster 3 consists of 10 earthquakes along a 40 km by 15 km planar region in the central Tonga slab (Fig. 2C). This cluster contains a pair of colocated events with M_w 5.6 and 5.4 that occurred within a time span of 2 hours on 12 September 1995 (Table 1).

Some of the colocated events may have resulted from repeated rupture on the same fault segment. We investigated the rupture extent of some of these events using an empirical Green's function (EGF) deconvolution method, in which smaller, short-duration events are used to remove wave propagation effects and recover the apparent source time function (*16*). A correction to the deconvolved time function is made to take into account the finite duration of the Green's function event itself, which is estimated by deconvolving an attenuation operator obtained from a regional attenuation model (*17*). The rise time ($\tau_{1/2}$), or time elapsed from the onset to the maximum of the source pulse, is then measured, and the fault radius is calculated from a quasi-dynamic model for a

circular rupture (*18*) with

$$r = \frac{\tau_{1/2} v_r}{1 - (v_r \sin\nu / c)} \quad (1)$$

where v_r is the velocity of the rupture, θ is the angle between the fault and the ray at the source, and c is the wave velocity (9.95 km/s). It is difficult to determine the rupture velocity for moderate-magnitude deep earthquakes. Large deep earthquakes generally show rupture velocities of 3 to 4.5 km/s, with the largest deep earthquakes in the Tonga-Fiji region showing rupture velocities of greater than 4 km/s (*10*, *19*). So we calculated the rupture radius assuming a rupture velocity of 3.8 km/s, corresponding to 70% of the shear velocity.

Results of these calculations show that the rupture zones of the closely spaced larger earthquakes overlap. In cluster 1, most of the 5 km by 15 km region along the upper part of the fault failed during two sequences on 14 February 1994 and 2 July 1994 (Fig. 3). The degree of fault overlap would be less if the earthquakes showed unusually low rupture velocity, but the ruptures of the 2 July double event would show some overlap even for rupture velocities as low as 1.4 km/s.

Clusters 2 and 3 also show several colocated series of events that represent repeated failure of the same fault surface. In particular, the two events in cluster 3 on 12 September 1995 are located at the same distance (2 km) and are of nearly the same magnitude as the 2 July events. EGF deconvolution suggests that the rupture radii of these events are similar to the 2 July events and thus would overlap. Cluster 2 also contains a region with four nearly identical events located within a 3 km by 2 km by 1 km volume, distributed randomly over the 2-year time period of the deployment.

Two earthquakes within a 55-s interval at 14:40:49 UT (M_w 4.8) and 14:41:44 (M_w 5.1) on 9 November 1994 suggest that even the spatial and temporal pattern of moment release may be repeated. The centroids of these events are closer than 2 km, and their positions cannot be distinguished at the 95% confidence level. Source pulses deconvolved with the EGF technique for these events show that each represents a double rupture and that the time history of the ruptures is nearly identical for the two events (Web fig. 1) (*20*). The time separation of the two pulses is 0.34 s for both events at station Lakeba, Fiji, and 0.40 and 0.44 s at Labasa, Fiji (Web fig. 1) (*20*). The similarity of the time functions at both widely separated stations suggests that the relative timing and position of the subevents are nearly identical for the two earthquakes. The average rise time of the pulses for the 14:40:49 event is 0.28 s and 0.35 s for the 14:41:44 event, suggesting rupture radii of 1.5 to 2 km for the subevents of both

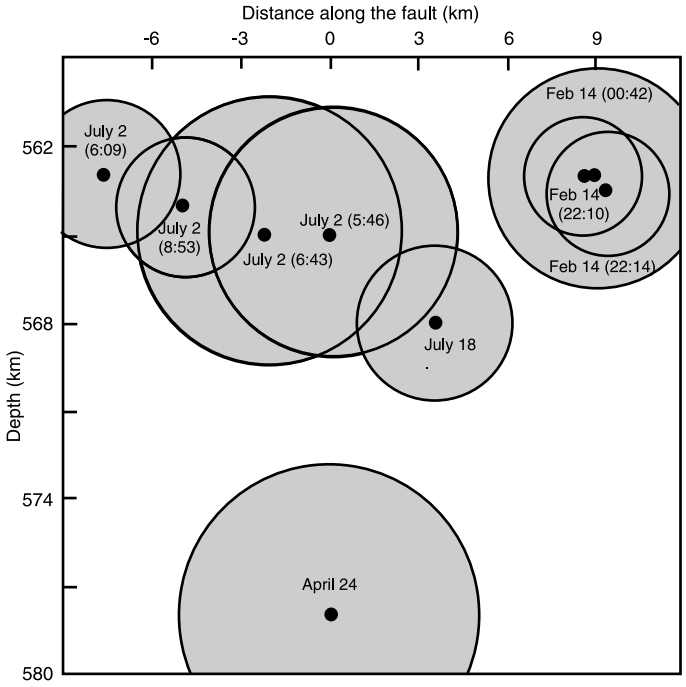

Fig. 3. Estimated rupture zones of earthquakes from cluster 1 assuming circular rupture. Rupture radius is calculated from the measured rise times determined by EGF deconvolution and assuming a rupture velocity of 3.8 km/s (70% of the shear velocity).

Table 1. Tonga colocated repeating events. Colocated events are defined as events located within 3 km, as determined with a waveform cross-correlation relative location method.

Cluster no.	Year	Month	Day	Hour	Minute	Second	Latitude	Longitude	Depth (km)	M_w	No. of arrivals	Uncertainty (km)
1	94	7	2	5	46	54.8	−20.90	−178.34	565.	5.6	32	0.9
1	94	7	2	6	9	5.4	−20.96	−178.39	563.	4.3	9	2.4
1	94	7	2	6	43	15.5	−20.92	−178.35	565.	5.5	28	1.1
1	94	7	2	8	53	23.5	−20.94	−178.37	564.	4.4	14	1.4
1	94	2	14	0	42	37.1	−20.82	−178.30	563.	5.0	14	1.4
1	94	2	14	22	10	49.0	−20.82	−178.31	563.	4.6	13	1.6
1	94	2	14	22	14	42.0	−20.81	−178.30	564.	4.4	10	2.1
2	94	11	9	14	40	49.6	−18.14	−178.14	604.	4.8	24	1.2
2	94	11	9	14	41	44.2	−18.13	−178.15	603.	5.1	28	0.9
2	94	10	7	12	54	48.6	−18.13	−178.14	596.	4.8	19	1.6
2	95	3	18	17	0	54.3	−18.14	−178.14	598.	5.0	15	1.9
2	94	2	17	22	40	56.7	−17.98	−178.26	580.	5.1	14	2.7
2	94	6	19	22	33	28.7	−17.98	−178.27	579.	4.8	13	2.5
2	95	1	9	19	50	6.2	−17.95	−178.28	580.	5.0	14	2.2
2	95	10	13	8	20	18.3	−17.96	−178.26	579.	4.8	17	2.9
2	95	5	25	16	45	58.4	−18.03	−178.18	586.	5.1	16	2.7
2	95	10	1	16	38	36.3	−18.04	−178.18	588.	4.9	20	2.2
3	95	9	12	12	44	41.2	−21.70	−179.00	594.	5.4	28	1.7
3	95	9	12	14	23	33.1	−21.68	−179.00	594.	5.6	28	1.5

earthquakes. These events represent four rupture events within a 2-km region during a time period of less than 1 min.

There is an important temporal element in the colocation of repeating ruptures, as four of the seven cases of colocated earthquakes recurred within a time span of less than 1 day (Table 1). The rate of subsequent earthquakes as a function of time after the initial earthquake in our data set is inversely proportional to time (Fig. 4), indicating that the tendency for recurrent faulting drops off rapidly with time, as does aftershock activity in general (*21*). However, this temporal association is not an aftershock phenomenon, as the seismic moments of the repeating events are similar to the initial event, whereas the largest deep earthquake aftershocks are generally about two orders of magnitude smaller than the mainshock (*22*). In addition, the high rate of repeating earthquakes observed in Tonga would be unexpected, given the low aftershock activity of deep earthquakes. The tendency for repeating deep earthquakes to show small recurrence times is much different from shallow repeating earthquakes, which show regular or semirandom distributions with time except in known aftershock zones (*4*).

Several mechanisms have been proposed to explain deep earthquakes, including transformational faulting (*6*, *8*, *23*), dehydration embrittlement (*7*, *24*), ductile shear zones (*25*), and fault zone melting (*9*). Previous studies suggest that repeating earthquakes would be incompatible with transformational faulting because a fault zone filled with transformed material would quickly strengthen due to grain size growth and become incapable of additional faulting (*6*). However, all faults and shear zones show a finite width, and the repeating earthquake data are compatible with rupture on parallel en-echelon faults that cannot be spatially resolved by the location procedure (within 1 to 2 km of each other). Laboratory data on transformational faulting suggest that the lens of transformed material ("the anticrack") has a small width relative to length (*26*). The presence of transformed material at the center of the fault zone inhibiting repeated faulting along the same plane is similar to strain hardening along shallow faults. Strain hardening leads to broadening of the shear zone as slip is transferred into the surrounding low-strength region (*27*); the same process could lead to en-echelon transformational faulting events adjacent to the initial one. In this model, the temporal dependence of the repeating earthquakes can result from either the time scale of the grain size growth in the anticrack or weakening of the surrounding region due to the latent heat of the original transformation event. However, the large rupture extent of the largest deep earthquakes and occurrence of aftershocks outside the active slab argue against the transformational faulting model (*7*, *10*, *15*).

Our preferred interpretation is that deep earthquakes represent runaway thermal events, either involving sudden ductile creep along a shear zone (*25*) or melting (*9*). Each of these strain-softening models would provide a logical mechanism for localizing repeated failures along the same fault. The seismically active structures imaged by the repeating earthquakes may represent deep shear zones that remain weak relative to the surrounding mantle because of lowered viscosity resulting from shear heating and from possible grain size reduction (*28*).

A deep shear zone would be expected to strengthen rapidly after catastrophic failure because of conductive cooling and the temperature-sensitive rheology, providing an explanation for the observed short recurrence time for repeating earthquakes. The rate of thermal diffusion can be estimated from the characteristic cooling time $t = x^2/\kappa$, where κ is the thermal diffusivity ($\sim 10^{-6}$ m^2/s) and x is one-half the thickness of the cooling zone (assuming that the fault cools from both sides). For a fault zone with a thickness of 1 m, the characteristic cooling time is on the order of 3 days, which can explain the short recurrence times of the deep earthquakes we have analyzed.

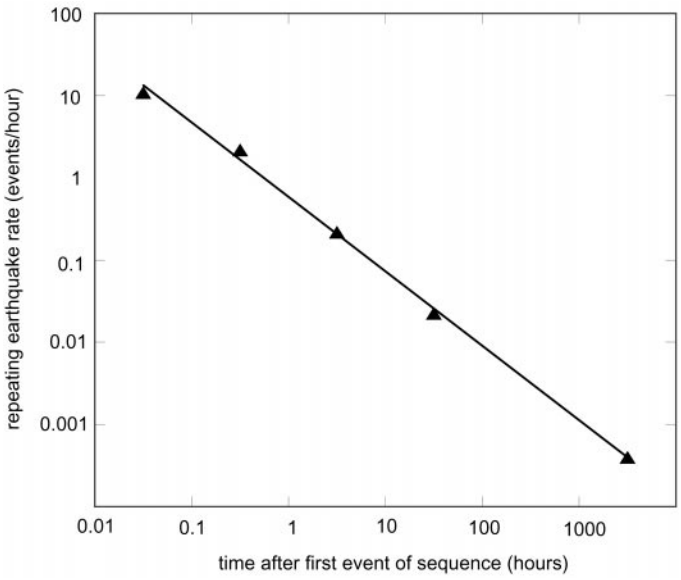

Fig. 4. Log-log plot of the rate of repeating earthquakes as a function of after the initial event of the sequence, taken from the data set of colocated events (Table 1). The line shows a linear least squares fit, in which the rate is proportional to $t^{-0.91}$, demonstrating that the repeating earthquakes show a strong preference for short recurrence intervals.

References and Notes

1. G. Poupinet, W. L. Ellsworth, J. Frechet, *J. Geophys. Res.* **89**, 5719 (1984).
2. P. M. Shearer, *J. Geophys. Res.* **102**, 8269 (1997); F. Waldhauser, W. L. Ellsworth, A. Cole, *Geophys. Res. Lett.* **26**, 3525 (1999); A. M. Rubin, D. Gillard, J.-L. Got, *Nature* **400**, 635 (1999); R. C. Aster, C. A. Rowe, in *Advances in Seismic Event Location*, C. Thurber, N. Rabinowitz, Eds. (Kluwer, Amsterdam, 2000), pp. 231–263.
3. J. E. Vidale, W. L. Ellsworth, A. Cole, C. Marone, *Nature* **368**, 624 (1994).
4. R. M. Nadeau, T. V. McEvilly, *Science* **285**, 718 (1999); D. P. Schaff, G. C. Beroza, B. E. Shaw, *Geophys. Res. Lett.* **25**, 4549 (1998).
5. B. L. Isacks, L. R. Sykes, J. Oliver, *Bull. Seismol. Soc. Am.* **57**, 935 (1967).
6. H. W. I. Green, H. Houston, *Annu. Rev. Earth Planet. Sci.* **24**, 169 (1995).
7. P. Silver *et al.*, *Science* **268**, 69 (1995).
8. S. H. Kirby, S. Stein, E. A. Okal, D. Rubie, *Rev. Geophys.* **34**, 261 (1996).
9. H. Kanamori, D. L. Anderson, T. H. Heaton, *Science* **279**, 839 (1998).
10. D. A. Wiens, *Phys. Earth Planet. Inter.*, in press.
11. D. A. Wiens *et al.*, *IRIS Newsl.* **14**, 1 (1995).
12. T. H. Jordan, K. A. Sverdrup, *Bull. Seismol. Soc. Am.* **71**, 1105 (1981).
13. D. Giardini, J. H. Woodhouse, *Nature* **307**, 505 (1984); P. R. Lundgren, D. Giardini, *Phys. Earth Planet Inter.* **74**, 63 (1992).
14. A. M. Dziewonski, T.-A. Chou, J. H. Woodhouse, *J. Geophys. Res.* **86**, 2825 (1981).
15. D. A. Wiens *et al.*, *Nature* **372**, 540 (1994).
16. S. H. Hartzell, *Geophys. Res. Lett.* **5**, 1 (1978).
17. E. G. Roth, D. A. Wiens, L. M. Dorman, J. Hildebrand, S. C. Webb, *J. Geophys. Res.* **104**, 4795 (1999).
18. J. Boatwright, *Bull. Seismol. Soc. Am.* **70**, 1 (1980).
19. M. Antolik, D. Dreger, B. Romanowicz, *J. Geophys. Res.* **104**, 863 (1999); R. Tibi, dissertation, Free University of Berlin (2000).
20. Web fig. 1 is available on *Science* Online at www.sciencemag.org/cgi/content/full/293/5534/1463/DC1.
21. C. Kisslinger, *Adv. Geophys.* **38**, 1 (1996).
22. D. A. Wiens, H. J. Gilbert, B. Hicks, M. E. Wysession, P. J. Shore, *Geophys. Res. Lett.* **24**, 2059 (1997).
23. H. W. Green, P. C. Burnley, *Nature* **341**, 733 (1989).
24. C. Meade, R. Jeanloz, *Science* **252**, 68 (1991).
25. B. E. Hobbs, A. Ord, *J. Geophys. Res.* **93**, 10521 (1988); M. Ogawa, *J. Geophys. Res.* **92**, 13801 (1987); S. Karato, M. R. Riedel, D. A. Yuen, *Phys. Earth Planet. Inter.*, in press.
26. H. W. Green, T. E. Young, D. Walker, C. H. Scholz, *Nature* **348**, 720 (1990).
27. J. Hull, *J. Struct. Geol.* **10**, 431 (1988); C. H. Scholz, *The Mechanics of Earthquakes and Faulting* (Cambridge Univ. Press, Cambridge, 1990).
28. M. Kameyama, D. A. Yuen, H. Fujimoto, *Geophys. Res. Lett.* **24**, 2523 (1997).

29. Regional seismic data were collected with equipment supplied by the PASSCAL program of the Incorporated Research Institutions in Seismology (IRIS). We thank R. Tibi and several anonymous reviewers for comments. This research was supported by the NSF.

1 June 2001; accepted 18 July 2001